Identification of Actin as a 15-Deoxy-$\Delta^{12,14}$-prostaglandin J_2 Target in Neuroblastoma Cells: Mass Spectrometric, Computational, and Functional Approaches To Investigate the Effect on Cytoskeletal Derangement†

Giancarlo Aldini,*,‡ Marina Carini,‡ Giulio Vistoli,‡ Takahiro Shibata,§ Yuri Kusano,§ Luca Gamberoni,‡ Isabella Dalle-Donne,|| Aldo Milzani,|| and Koji Uchida§

Istituto di Chimica Farmaceutica e Tossicologica "Pietro Pratesi", Faculty of Pharmacy, University of Milan, I-20131 Milan, Italy, Graduate School of Bioagricultural Sciences, Nagoya University, Nagoya 464-8601, Japan, and Department of Biology, University of Milan, I-20133 Milan, Italy

Received September 6, 2006; Revised Manuscript Received January 3, 2007

ABSTRACT: A proteomic approach was used to identify 15-deoxy-$\Delta^{12,14}$-prostaglandin J_2 (15d-PGJ_2) protein targets in human neuroblastoma SH-SY5Y cells. By using biotinylated 15d-PGJ_2, β-actin was found as the major adducted protein; at least 12 proteins were also identified as minor biotin-positive spots, falling in different functional classes, including glycolytic enzymes (enolase and lactate dehydrogenase), redox enzymes (biliverdin reductase), and a eukaryotic regulatory protein (14-3-3γ). 15d-PGJ_2 induced marked morphological changes in the actin filament network and in particular promoted F-actin depolymerization as confirmed by Western blot analysis. By using a mass spectrometric approach, we found that 15d-PGJ_2 reacts with isolated G-actin in a 1:1 stoichiometric ratio and selectively binds the Cys374 site through a Michael adduction mechanism. Computational studies showed that the covalent binding of 15d-PGJ_2 induces a significant unfolding of actin structure and in particular that 15d-PGJ_2 distorts the actin subdomains 2 and 4, which define the nucleotide binding sites impeding the nucleotide exchange. The functional effect of 15d-PGJ_2 on G-actin was studied by polymerization measurement: in the presence of 15d-PGJ_2, a lower amount of F-actin forms, as followed by the increase in pyrenyl-actin fluorescence intensity, as the major effect of increasing 15d-PGJ_2 concentrations occurs on the maximum extent of actin polymerization, whereas it is negligible on the initial rate of reaction. In summary, the results here reported give an insight into the role of 15d-PGJ_2 as a cytotoxic compound in neuronal cell dysfunction. Actin is the main protein cellular target of 15d-PGJ_2, which specifically binds through a Michael adduction to Cys374, leading to a protein conformational change that can explain the disruption of the actin cytoskeleton, F-actin depolymerization, and impairment of G-actin polymerization.

The prostaglandins (PGs)[1] are a family of structurally related molecules that are produced by cells in response to a variety of extrinsic stimuli and that regulate cellular growth, differentiation, and homeostasis (*1*, *2*). PGs are derived from fatty acids, primarily arachidonate, which are released from membrane phospholipids by the action of phospholipases. Arachidonate is first converted to an unstable endoperoxide intermediate by cyclooxygenases and then is subsequently converted to one of several related products, including PGD_2, PGE_2, $PGF_{2\alpha}$, prostacyclin (PGI_2), and thromboxane A_2, through the action of specific PG synthetases. PGD_2 is a major cyclooxygenase-catalyzed reaction product in a variety of tissues and cells and has significant effects on a number of biological processes, including platelet aggregation, the relaxation of vascular and nonvascular smooth muscles, and nerve cell functions (*3*).

It has also been shown that PGD_2 readily undergoes dehydration in vivo and in vitro to yield biologically active PGs of the J_2 series, such as PGJ_2, Δ^{12}-PGJ_2, and 15-deoxy-$\Delta^{12,14}$-PGJ_2 (15d-PGJ_2) (Figure 1) (*4*). Members of the J_2 series of the PGs, unlike other classes of eicosanoids characterized by the presence of an electrophilic α,β-unsaturated carbonyl group in the cyclopentenone ring, have their own unique spectrum of biological effects, including inhibition of macrophage-derived cytokine production (*5*, *6*) and IκB kinase (*7*, *8*), induction of synoviocyte and endo-

† This study was supported by COFIN 2004 (Cofinanziamento Programma Nazionale 2004) and FIRST 2005 (Fondo Interno Ricerca Scientifica e Tecnologica, University of Milan).

* To whom correspondence should be addressed. Tel: +39-02-50317545. Fax: +39-02-50317565. E-mail: giancarlo.aldini@unimi.it.

‡ Istituto di Chimica Farmaceutica e Tossicologica Pietro Pratesi, University of Milan.

§ Graduate School of Bioagricultural Sciences, Nagoya University.

|| Department of Biology, University of Milan.

[1] Abbreviations: PGs, prostaglandins; PGI_2, prostacyclin; 15d-PGJ_2, 15-deoxy-$\Delta^{12,14}$-PGJ_2; IκB, inhibitor κ B; LC-ESI-MS/MS, liquid chromatography−electrospray ionization tandem mass spectrometry; DTT, (±)-*threo*-1,4-dimercapto-2,3-butanediol; LC, liquid chromatography; ECL, enhanced chemiluminescence; EDC, 1-ethyl-3-(dimethylaminopropyl)carbodiimide; FBS, fetal bovine serum; PBS, phosphate-buffered saline; BSA, bovine serum albumin; EDTA, ethylenediaminetetraacetic acid; SDS−PAGE, sodium dodecyl sulfate−polyacrylamide gel electrophoresis; MALDI-TOF, matrix-assisted laser desorption ionization−time of flight; PIPES, piperazine-1,4-bis(2-ethanesulfonic acid); EGTA, ethylene glycol bis(2-aminoethyl ether)tetraacetic acid; IEF, one-dimensional isoelectric focusing; TBS, Tris-buffered saline; TFA, trifluoroacetic acid; MS, mss spectrometry; GSH, glutathione; ESI-MS, electrospray ionization−mass spectrometry; HNE, 4-hydroxy-*trans*-2-nonenal; TCA, trichloroacetic acid; MD, molecular dynamics; RMSD, root mean square deviation.

10.1021/bi0618565 CCC: $37.00
Published on Web 02/13/2007

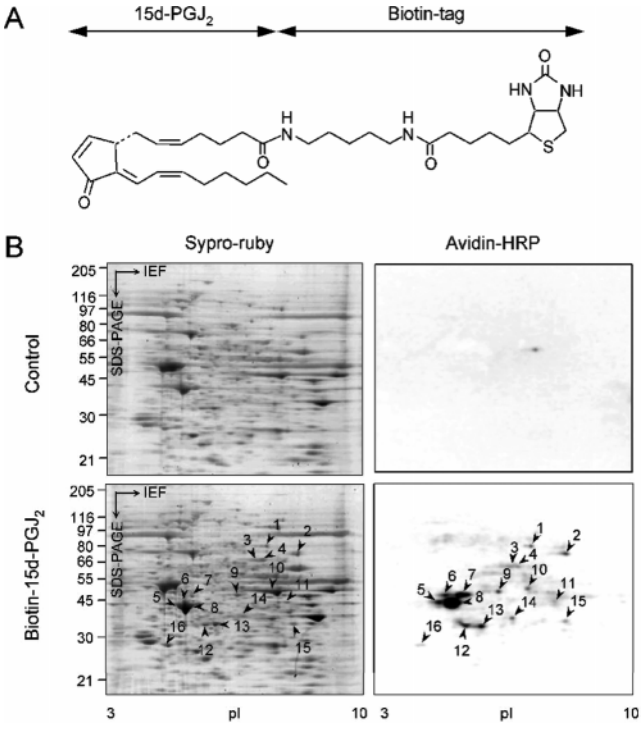

FIGURE 1: Identification of biotinylated 15d-PGJ_2-modified proteins in SH-SY5Y cells. (A) Chemical structure of biotinylated 15d-PGJ_2. (B) SH-SY5Y cells were incubated with 10 μM biotinylated 15d-PGJ_2 for 2 h. The proteins were separated by isoelectrofocusing (pH range 3−10) and then by SDS−PAGE. Left panel: SYPRO Ruby fluorescence staining. Right panel: Western blot. The arrowheads denote spots excised for subsequent identification by MALDI-TOF analysis, as described under Experimental Procedures.

thelial cell apoptosis (*9*), induction of glutathione *S*-transferase gene expression (*10*), and potentiation of apoptosis in neuronal cells (*11*). Moreover, recent studies have shown that 15d-PGJ_2 directly inhibits the NF-κB-dependent gene expression through covalent modification of critical cysteine residues in IκB kinase (*7*) and the DNA-binding domains of NF-κB subunits (*8*, *12*).

We have recently shown that 15d-PGJ_2 induces apoptosis of SH-SY5Y human neuroblastoma cells via accumulation of p53. Moreover, the Fas/Fas ligand pathway has been identified as the downstream signaling mechanism in the p53-mediated apoptosis (*11*). Moreover, it has been shown that 15d-PGJ_2 is accumulated in the spinal cord of sporadic amyotrophic lateral sclerosis (ALS) patients, mainly occurring in the motor neurons of the anterior horn (*11*). In the present study, to gain an insight into the role of 15d-PGJ_2 modification of protein in the neuronal cell dysfunction, we used a proteomic approach to identify the significantly 15d-PGJ_2-modified proteins in human neuroblastoma SH-SY5Y cells and identified β-actin as the major molecular target for the covalent modification by 15d-PGJ_2. The molecular mechanism for cysteine-targeted modification of this cytoskeletal protein and the effects of actin modification by 15d-PGJ_2 on protein polymerization were elucidated by a combined computational, functional, and mass spectrometric approach.

EXPERIMENTAL PROCEDURES

Chemicals. 15-Deoxy-$\Delta^{12,14}$-prostaglandin J_2 (15d-PGJ_2) and 9,10-dihydro-15d-PGJ_2 were obtained from Cayman Chemicals (Ann Arbor, MI; Cabru, Milan, Italy), and iodoacetamide, (±)-*threo*-1,4-dimercapto-2,3-butanediol (DTT), and ATP (disodium salt) were from Sigma-Aldrich (Milan, Italy). Sequence grade modified trypsin was purchased from Promega (Madison, WI; Milan, Italy), and *N*-(1-pyrenyl)-iodoacetamide was from Molecular Probes (Eugene, OR). LC grade and analytical grade organic solvents were purchased from Merck (Bracco, Milan, Italy). LC grade water was prepared with a Milli-Q water purification system (Millipore, Bedford, MA). All other reagents were of analytical grade. Horseradish peroxidase-linked anti-goat IgG immunoglobulins and enhanced chemiluminescence (ECL) Western blotting detection reagents were obtained from DakoCytomation (Glostrup, Denmark) and GE Healthcare Bio-Sciences Corp. (Piscataway, NJ), respectively. The antibody against β-actin was obtained from Santa Cruz Biotechnology (Santa Cruz, CA). The protein concentration was measured using the BCA protein assay reagent obtained from Pierce (Rockford, IL). UltraLink Immobilized NeutrAvidin Plus and 1-ethyl-3-(dimethylaminopropyl)carbodiimide (EDC) were obtained from Pierce.

Cell Culture. Human neuroblastoma SH-SY5Y cells were grown in Cosmedium-001 (Cosmo-Bio, Tokyo, Japan) containing 5% FBS. The cells were seeded in plates coated with polylysine and cultured at 37 °C.

Preparation of Biotinylated 15d-PGJ_2. The carboxyl group of 15d-PGJ_2 was modified by amidation with EZ-link 5-(biotinamido)pentylamine (Pierce) by a modification of a previously described procedure (*12*). Biotinylated 15d-PGJ_2 was purified through a reverse-phase HPLC eluted with a linear gradient of acetonitrile−water−acetic acid (80:20:0.01 v/v/v) (solvent A) and acetonitrile−acetic acid (100:0.01 v/v) (solvent B) (time = 0 min, 100% A; 50 min, 0% A). The modified PG was then dried under argon and dissolved in DMSO for further use.

Fluorescence Microscopy of Actin Filaments. SH-SY5Y cells were treated with DMSO (vehicle control), 1 μM cytochalasin D, or 20 μM 15d-PGJ_2 for 2 h and then fixed in PBS containing 3.8% paraformaldehyde for 30 min. The membranes were permeabilized by exposing the fixed cells to cold acetone. The cells were then sequentially incubated in PBS solutions containing 2% BSA. The cells were then incubated overnight in the presence of Alexa Fluor 488 phalloidin (Molecular Probes Inc., Eugene, OR), rinsed with PBS, and covered with antifade solution. Images of the cellular immunofluorescence were acquired using a confocal laser scanning microscope (LSM5 PASCAL; Zeiss).

Biotinylated 15d-PGJ_2 Labeling of Actin in SH-SY5Y Cells. SH-SY5Y cells at 50% confluence were incubated with 10 μM biotinylated 15d-PGJ_2 for 2 h. The cells were washed with PBS, harvested, and lysed in 10 mM Tris-HCl (pH 7.4), 1 mM EDTA, 0.1% SDS, and 1% Triton, plus protease inhibitors. Cell lysates containing 200 μg of protein were incubated batchwise with 50 μL of NeutrAvidin-Plus beads overnight at 4 °C with constant shaking. The beads were rinsed three times with lysis buffer by centrifugation at 3000 rpm for 1 min. The proteins were eluted by boiling the beads in Laemmli sample buffer for 5 min and analyzed by SDS−PAGE followed by immunodetection with anti-actin antibody. In addition, the cell lysates were incubated with 3 μg of anti-actin antibody overnight at 4 °C. The mixture was then treated with 50 μL of protein G−Sepharose (GE

Healthcare Bio-Sciences) and incubated for 1 h at 4 °C. The mixture was then centrifuged (2000 rpm, 5 min), rinsed three times with lysis buffer, and then boiled with the Laemmli sample buffer, and the biotinylated proteins were then subjected to immunoblot and detection with HRP-conjugated streptavidin and ECL.

Protein Separation by Two-Dimensional Electrophoresis. Two-dimensional electrophoresis was performed with the ZOOM IPG runner system (Invitrogen). Before electrophoresis was performed, the samples were dialyzed with a 2D clean-up kit (GE Healthcare Bio-Sciences). The samples containing 150 μg of total cell lysate were dissolved in a rehydration buffer (8 M urea, 2% CHAPS, 0.5% ZOOM carrier ampholytes, 0.002% bromophenol blue, and 20 mM DTT) for one-dimensional isoelectric focusing (IEF). The pH range of the IEF was 3−10. After IEF was performed, the gel strips were incubated with NuPAGE LDS sample buffer. For two-dimensional electrophoresis, NuPAGE 4−12% BisTris ZOOM gel was used. All procedures followed the manufacturer's protocol. Separated proteins were then fixed in the gel using 40% ethanol and 10% formic acid, stained with SYPRO Ruby protein gel stain, and scanned using the Typhoon 9400 (GE Healthcare Bio-Sciences). The protein spots were visualized by Image Quant (GE Healthcare Bio-Sciences). For immunoblotting, gels were transferred to nitrocellulose membranes (GE Healthcare Bio-Sciences). The membranes were incubated with Block Ace (40 mg mL^{-1}) for blocking and washed with TBS containing 0.05% Tween-20 (TBS/Tween). This procedure was followed by the addition of HRP-conjugated streptavidin and ECL reagents (GE Healthcare Bio-Sciences). The spots were visualized by LumiVision PRO 400EX (Aisin Seiki Co., Ltd., Aichi, Japan).

Identification of 15d-PGJ$_2$-Modified Proteins. Gel pieces were washed in water containing 0.1% and 50% methanol for 1 h, dehydrated in acetonitrile, and dried in a SpeedVac for 30 min. Samples were proteolyzed with 1 μg of sequence grade modified trypsin in 100 mM Tris-HCl buffer (pH 8.8) overnight at 37 °C. The supernatant was collected, and peptides were further extracted with 50% acetonitrile containing 0.1% TFA. Peptide extracts were vacuum-dried and resuspended in 50% acetonitrile containing 0.1% formic acid. Peptide mass fingerprints were generated with an ABI 4700 Proteomics Analyzer matrix-assisted laser desorption ionization−time-of-flight−time-of-flight (MALDI-TOF-TOF) mass spectrometer (Applied Biosystems, Foster City, CA). A few microliters of the sample was mixed with an equal volume of a saturated solution of sinapinic acid or α-cyano-4-hydroxycinnamic acid (Sigma) in acetonitrile/0.1% trifluoroacetic acid 1:3 (v/v); 1 μL of the mixture was deposited on the MALDI-TOF mass spectrometry target. Proteins were identified with the MASCOT (Matrix Science, London) searching algorithms using the NCBInr database. Probability-based MOWSE scores were estimated by comparison of search results against estimated random match population and were reported as ~10 log 10(p), where p is the absolute probability. Scores greater than 40 were considered significant, meaning that for scores higher than 40 the probability that the match is a random event is lower than 0.05. All protein identifications were in the expected size and PI range based on position in the gel.

Preparation of F- and G-Actin Extracts. SH-SY5Y cells were treated with DMSO (vehicle control), 1 μM cytochalasin, or 20 μM 15d-PGJ$_2$ for 2 h, then rinsed with phosphate-buffered saline at 25 °C, and scraped and homogenized in a lysis and F-actin stabilization buffer (250 mM PIPES buffer, pH 6.9, 1 mM ATP, 50 mM NaCl, 5 mM $MgCl_2$, 5 mM EGTA, 5% glycerol, 0.1% Nonidet P-40 (NP40), 0.1% Triton X-100, 0.1% Tween-20, 0.1% β-mercaptoethanol, 0.001% antifoam, and protease inhibitors). F-actin was then separated from G-actin by centrifugation at 100000g for 60 min at 37 °C. The F-actin-containing pellet was resuspended in doubly distilled H_2O containing 2 μM cytochalasin D at a volume equivalent to the G-actin-containing supernatant volume. The resuspended F-actin pellet was kept on ice for 60 min with mixing by pipet every 15 min to dissociate F-actin. After dissociation, dissociated F-actin was centrifuged at 14000g for 10 min at 4 °C.

G-Actin Preparation. Rabbit skeletal muscle actin was prepared as previously described (*13*). G-actin in 2 mM Tris-HCl, pH 7.5, 0.5 mM DTT, 0.2 mM ATP, 0.2 mM $CaCl_2$, and 1.5 mM NaN_3 (buffer G) was lyophilized after the addition of 2 mg of sucrose/mg of actin and stored at −20 °C. To prepare G-actin, the lyophilized powder was dissolved and dialyzed for at least 24 h against buffer G depleted of DTT (buffer A). G-actin (molecular mass 42.3 kDa) concentration was determined by measuring the absorbance at 290 nm, using an extinction coefficient of 0.63 mg^{-1} mL cm^{-1}. *N*-(1-Pyrenyl)iodoacetamide-labeled actin (pyrene-actin) was prepared as previously described (*13*). The pyrene-actin concentration and the extent of labeling were determined by measuring the absorbance at 290 and 344 nm, by using $\epsilon_{344} = 2.2 \times 10^4$ M^{-1} cm^{-1} for the protein−dye complex (*14*, *15*). Prior to use, G-actin solutions were clarified by a 30 min centrifugation at 180000g. Before sample preparation, protein solutions and buffers were filtered with 0.20 μm disposable filters and degassed.

In Vitro Modification of G-Actin by 15d-PGJ$_2$. Isolated G-actin, solubilized in buffer A at a final concentration of 20 μM, was treated with 15d-PGJ$_2$ at a final G-actin:15d-PGJ$_2$ molar ratio of 1:5, 1:10, and 1:20 (2 mL final volume). After an incubation period of 60 min at 37 °C, 1 mL aliquots were immediately subjected to polymerization measurements, and the remaining were stabilized by 5 mM $NaBH_4$ (60 min at room temperature) for MS analyses. The samples were then desalted by Microcon YM-30 centrifugal filter devices (Millipore, Milan, Italy), lyophilized, and stored in liquid nitrogen until MS analyses.

Preparation of the GSH−15d-PGJ$_2$ Conjugate. Standard of the GSH−15d-PGJ$_2$ conjugate was prepared by incubating equimolar concentrations of GSH and 15d-PGJ$_2$ (400 μM) at 37 °C for 24 h in 1 mM phosphate buffer, pH 7.2. The reduced form of 15d-PGJ$_2$−GSH was obtained by $NaBH_4$ treatment (5 mM final concentration) for 60 min at room temperature. The identity of the standard was verified by ESI-MS analysis (direct infusion) in both positive and negative ion modes.

Polymerization Measurements. G-actin polymerization was monitored by measuring the fluorescence enhancement of trace quantities of pyrene-actin (10% of 10 μM total actin) in a thermostated cuvette at 25 °C. The spectrofluorometer was equipped with a neutral density filter (50%), to avoid pyrene-actin photobleaching, and a cutoff filter (390 nm),

to minimize the contribution of light scattering to the data. The excitation and emission wavelengths were 365 and 407 nm, respectively. Fluorescence intensities were expressed in percentage, considering 100% the signal from a standard sample (10 μM G-actin polymerized by 100 mM KCl and 2 mM $MgCl_2$ at 25 °C) when no further changes in fluorescence intensity were observed.

Direct Infusion Electrospray Mass Spectral Analysis (ESI-MS): Triple Quadrupole (TQ) Mass Spectrometer. To detect changes in protein mass and to determine the stoichiometry of reaction, undigested native and 15d-PGJ_2-treated actin were analyzed by direct infusion on a triple quadrupole mass spectrometer (Finnigan TSQ Quantum Ultra; ThermoQuest, Milan, Italy) equipped with an electrospray Finnigan ion max source. Lyophilized protein (420 μg) was dissolved in 200 μL of water, mixed with 200 μL of water−acetonitrile−formic acid (70:30:0.4 v/v/v), and infused into the mass spectrometer at a flow rate of 5 μL min^{-1}. Each sample was analyzed using two different mass ranges: *m*/*z* 600−1500 ($Q = m/z$ 1) and *m*/*z* 1310−1420 ($Q = m/z$ 0.5), under the following instrumental conditions: positive ion mode; heated capillary temperature, 220 °C; electrospray needle, 5 kV; capillary voltage, 46 V. The nitrogen (the nebulizer gas) flow rate was set at 0.5 L min^{-1}; acquisition time 10 min.

Liquid Chromatography Electrospray Ionization Mass Spectrometry/Mass Spectrometry Analysis (LC-ESI-MS/MS): Ion Trap Mass Spectrometer. Tryptic peptide maps were generated by LC-ESI-MS/MS analysis in data-dependent scan mode and dynamic exclusion in both positive and negative ion modes. For sample preparation, lyophilized target protein (420 μg) was dissolved in 100 μL of 50 mM Tris-HCl (pH 7.8) containing 6 M urea and DTT (5 μL of a 200 mM solution) and heated at 60 °C for 60 min. Cysteinyl thiols were then blocked by the addition of iodoacetamide (20 μL of a 200 mM solution) for 60 min in the dark at room temperature. Residual iodoacetamide was quenched by addition of 20 μL of DTT and incubation for an additional 60 min in the dark. The sample was then diluted to 1 mL with 50 mM NH_4HCO_3 (pH 7.8), and a 200 μL aliquot was digested with trypsin at a protease:protein ratio of 1:20 (w/w) for 24 h at 37 °C. To terminate the protease activity, samples were ultrafiltered by using Centricon Ultracel YM-10 (Millipore, Milan, Italy) according to the supplier's protocol. The filtrate (100 μL) was injected into a quaternary pump HPLC system (Surveyor LC system; ThermoQuest, Milan, Italy). Sample desalting and concentration were carried out on-line using an Opti-Lynx C18 (40 μm) trap cartridge (El-Chimie srl; Bresso, Milan, Italy) installed in the rheodyne injection valve loop. Separations were done by reversed-phase elution with an Agilent Zorbax SB-C18 column (4 mm i.d., particle size 3.5 μm) (CPS Analitica, Milan, Italy) protected by an Agilent Zorbax R-P guard column, thermostated at 25 °C. After a 5 min isocratic elution with phase A (0.1% formic acid in water; divert valve opened), the following gradient program (165 min) was used to elute the digested peptides: (a) from 100% solvent A to 40% solvent B (acetonitrile−water−formic acid, 90:10:0.1 v/v/v) in 75 min; (b) isocratic elution for an additional 50 min; (c) from 40% to 100% solvent B within 40 min to return at 100% solvent A at 171 min. The equilibration period was set to 14 min, and the mobile phase was delivered at a flow rate of 0.2 mL min^{-1}.

The ESI-MS (Finnigan LCQ Advantage Ion trap mass spectrometer; ThermoQuest, Milan, Italy) was set in both positive and negative ion modes under the following conditions: capillary temperature 250 °C; spray voltage 4.5 kV; source current 10 μA; capillary voltage 10.0 V. The flow rate of the nebulizer gas (nitrogen) was 5 L min^{-1}. Standards of the GSH−15d-PGJ_2 conjugate and of the corresponding reduced form were analyzed by LC-ESI-MS/MS in the same conditions as above reported, except for the injected volume (10 μL).

Bioinformatics. Direct infusion ESI-MS spectra were deconvoluted using the software package Bioworks 3.1 (ThermoQuest, Milan, Italy) and MagTran 1.02 (*16*). Peptide sequences were identified using the software turboSEQUEST (Bioworks 3.1; ThermoQuest, Milan, Italy) and using a database containing only the protein of interest and assuming trypsin digestion. In silico tryptic digest of actin was also used as an aid for peptide identification. The protein sequence of α-actin from skeletal muscle was obtained from the SWISS-PROT database (primary accession number P68136). PEPTIDEMASS (*17*) was used to calculate theoretical digested masses based on the tryptic digest and setting all Cys as (carbamidomethyl)cysteine. Predicted y and b series ions were determined by using the Peptide Sequence Fragmentation Modeling, Molecular Weight Calculator software program (version 6.37), http://come.to/alchemistmatt. Xcalibur software provided instrument control and data analysis for the Thermo Electron mass spectrometers.

Computational Studies. The minimized structure of native ATP actin monomer was generated as previously described (*18*) using the crystal structure of monomeric actin in the ATP state (PDB Id 1NWK). The 15d-PGJ_2 conformation was obtained by extracting the structure of PGD_2 from the crystal structure of PGF synthase complexed with PGD_2 (PDB Id 1RYO) and manually transforming the PGD_2 in 15d-PGJ_2, using VEGA software (*19*). The actin structure was used to build both isomers of the 15d-PGJ_2 covalent Michael adduct at C_9 on the thiol group of Cys374. The adducts were solvated by a solvent sphere with a radius of 40 Å around the protein, and a spherical boundary condition (radius = 50 Å) was applied to stabilize the water cluster. Before the MD simulations were performed, the complexes were also optimized for the relative position of the solvent molecules to eliminate any high-energy interaction. The obtained systems underwent to a 5 ns MD simulation with the following characteristics: constant temperature at 300 ± 10 K by means of Langevin's algorithm; Lennard-Jones (L-J) interactions were calculated with a cutoff of 10 Å, and the pair list was updated every 20 iterations; Newton's equation was integrated, using the r-RESPA method, every 4 fs for long-range electrostatic forces, 2 fs for short-range nonbonded forces, and 1 fs for bonded forces; a frame was stored every 5 ps, yielding 1000 frames. The simulations were carried out in two phases: an initial period of heating from 0 to 300 K over 3000 iterations (3 ps, i.e., 1 K/10 iterations) and the monitored phase of simulation of 5 ns. Only frames memorized during this last phase were considered. In all simulations, only the Ca^{2+} ions were kept fixed. The same computational protocol was also used to perform a 5 ns MD simulation on native actin.

Table 1: Summary of 15d-PGJ$_2$-Modified Proteins

no.	accession no.	protein name	MW	PI	total ion score	sequence coverage (%)	peptide
1	gi|15082535	guanine monophosphate synthetase	76667	6.42	41	16	9
2	gi|37267	transketolase	67844	7.90	73	6	3
3		ND					
4		ND					
5	gi|15277503	ACTB protein (β-actin)	40194	5.55	201	15	4
6	gi|5902734	actin	41563	5.30	89	9	2
7	gi|16198386	eukaryotic translation initiation factor 4A, isoform 2	46346	5.33	112	10	3
8	gi|15277503	ACTB protein (β-actin)	40194	5.55	313	26	5
9		ND					
10	gi|62896593	enolase 1 variant	47111	7.01	85	14	3
11		ND					
12	gi|55962250	pyrophosphatase (inorganic)	32639	5.54	84	7	2
13	gi|49259212	chain D, human B lactate dehydrogenase	36516	5.86	91	15	4
14	gi|13543489	biliverdin reductase A	33411	6.06	66	8	2
15	gi|6680047	guanine nucleotide binding protein (G protein), β polypeptide 2-like 1 variant	35055	7.60	68	6	2
16	gi|5726310	14-3-3 γ protein	28357	4.66	48	10	3

RESULTS

Identification of β-Actin as the Major Target of 15d-PGJ$_2$. We prepared a biotinylated 15d-PGJ$_2$ (Figure 1A), which retains the α,β-unsaturated ketone substituent and the electrophilic β-carbon of 15d-PGJ$_2$. To identify targets of 15d-PGJ$_2$ in the cells, the SH-SY5Y cells were treated with 10 μM biotinylated 15d-PGJ$_2$ for 2 h, and the 15d-PGJ$_2$-protein conjugates were separated on two-dimensional gel electrophoresis and analyzed by Western blot analysis probed with streptavidin−HRP. As shown in Figure 1B, several 15d-PGJ$_2$-protein conjugates were detected following biotinylated 15d-PGJ$_2$ treatment. Spots were then excised from two-dimensional gels, subjected to trypsin digestion, and then successfully analyzed by MALDI-TOF mass fingerprint analysis. The multiple gel spots for a single identification may be due to posttranslational modification, such as phosphorylation. However, at this moment, it is impossible by visual inspection of a pattern of spots on a gel to determine which modifications are most likely to be present. Spot 8 corresponding to a 40 kDa 15d-PGJ$_2$−protein conjugate was one of the major targets of the modification by biotinylated 15d-PGJ$_2$, as seen in Figure 1B. Using MASCOT, the provability based MOWSE score was 313 for β-actin ($p < 0.05$), with five peptide matches (error $\pm$ 0.01%), which represents 26% sequence coverage. Table 1 lists the identity of 12 protein spots, which could be identified in one or more of three independent experiments. The identified proteins fall into several different functional classes, including glycolytic enzymes (enolase and lactate dehydrogenase), redox enzymes (biliverdin reductase), and a eukaryotic regulatory protein (14-3-3 protein).

Covalent Binding of 15d-PGJ$_2$ to Endogenous β-Actin in SH-SY5Y Cells. We then attempted to detect the 15d-PGJ$_2$−actin adduct in the cells exposed to the biotinylated 15d-PGJ$_2$. To this end, the SH-SY5Y cells were treated with 10 μM biotinylated 15d-PGJ$_2$ for 2 h, and the cell lysate was incubated with NeutrAvidin beads. After being washed with lysis buffer, proteins bound to the resin through biotinylated 15d-PGJ$_2$ were eluted with SDS−PAGE sample buffer, and β-actin was detected by immunoblot analysis with the anti-β-actin antibody (Figure 2A). Alternatively, cell lysates were subjected to immunoprecipitation with an anti-β-actin antibody, and the presence of biotinylated 15d-PGJ$_2$-modified proteins was detected by immunoblot analysis with HRP-conjugated avidin (Figure 2B). Thus, it appeared that 15d-PGJ$_2$ covalently reacted with endogenous β-actin, itself, in intact SH-SY5Y cells.

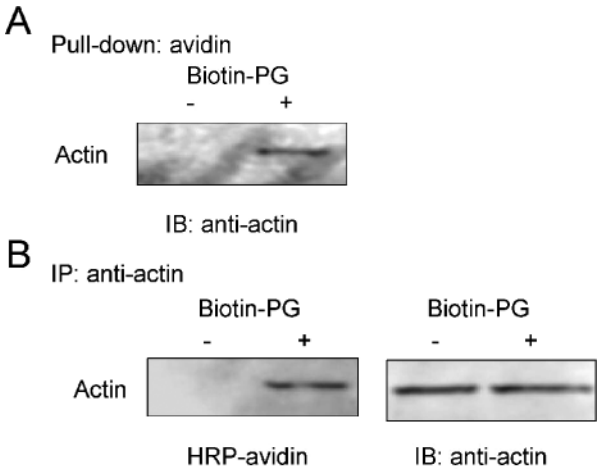

FIGURE 2: Interaction between actin and 15d-PGJ$_2$ in intact SH-SY5Y cells. SH-SY5Y cells were treated with 10 μM biotinylated 15d-PGJ$_2$ for 2 h. Cell lysates were incubated with immobilized NeutrAvidin (A) or with anti-actin−Sepharose (B). The presence of actin was detected by immunoblot analysis, and the incorporation of biotinylated 15d-PGJ$_2$ into actin immunoprecipitates was detected with HRP-avidin and ECL.

Disruption of the Actin Cytoskeleton by 15d-PGJ$_2$. We examined the organization of actin filaments in SH-SY5Y cells. The actin cytoskeleton in the nontreated control cells comprised a stress fiber-like structure or thick struts of actin fiber extended across the length of the neuronal cells (Figure 3A, panels a and b). Incubation of SH-SY5Y cells with 1 μM cytochalasin D and 20 μM 15d-PGJ$_2$ for 2 h induced marked morphologic changes in the actin filament network (Figure 3A, panels c−f). It is interesting that 9,10-dihydro-15d-PGJ$_2$, an analogue of 15d-PGJ$_2$ that lacks the cyclopentenone moiety and displays reduced ability to bind to proteins, did not induce actin redistribution (data not shown), thus suggesting that thiol modification is important for the effects of 15d-PGJ$_2$ on SH-SY5Y cell cytoskeletal organization. In addition, F-actin determination by Western blot analysis confirmed that cells incubated with 15d-PGJ$_2$

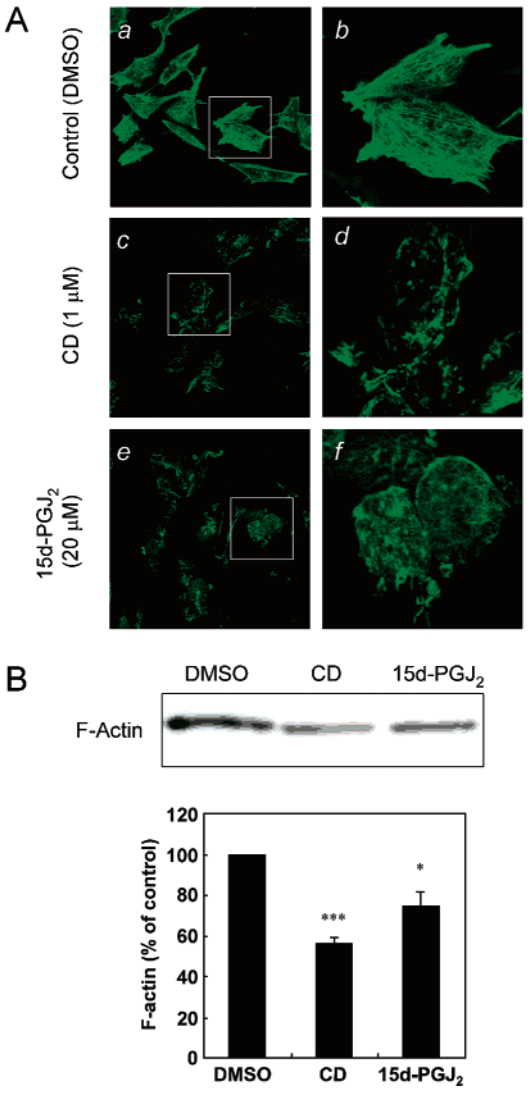

FIGURE 3: Disruption of the actin cytoskeleton by 15d-PGJ_2. (A) SH-SY5Y cells were treated with DMSO (panels a and b), 1 μM cytochalasin D (CD) (panels c and d), or 20 μM 15d-PGJ_2 (panels e and f), as indicated, and stained with phalloidin to visualize filamentous actin. Lower magnification: panels a, c, and e. Higher magnification: panels b, d, and f. (B) F-actin fractions were prepared, resolved on a 10% polyacrylamide gel, and subjected to Western blotting with anti-actin antibody. The results are representative of three separate experiments. Quantitative analysis of relative F-actin levels is shown in the lower panel. Results show the mean ± SEM of three experiments. *, $p < 0.05$; ***, $p < 0.005$ versus vehicle control (DMSO).

undergo a reduction in F-actin (Figure 3B), consistent with an induced depolymerization of cortical F-actin.

G-Actin Polymerization. The kinetics of G-actin assembly is shown in Figure 4. In the presence of 15d-PGJ_2−actin adducts, a lower amount of F-actin forms, as followed by the increase in pyrenyl-actin fluorescence intensity, as the major effect of increasing 15d-PGJ_2 concentrations occurs on the maximum extent of actin polymerization, whereas it is negligible on the initial rate of reaction. The time ($t_{1/2}$) required for half-maximum assembly was 4.2 min in control and 7.0, 7.5, and 10.2 min in G-actin exposed to a 1:5, 1:10, or 1:20 actin:15d-PGJ_2 molar ratio, respectively. Furthermore, exposure of G-actin to 15d-PGJ_2 alters the extent (i.e., the apparent equilibrium) of polymerization, during which the fluorescence intensity is constant. Polymerization extent

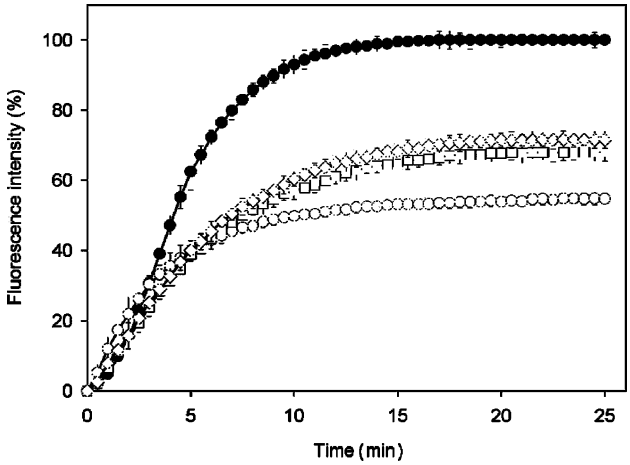

FIGURE 4: Time course of actin filament formation in native and 15d-PGJ_2-treated actin. Changes in fluorescence intensity were monitored immediately after the addition of 100 mM KCl + 2 mM $MgCl_2$ to G-actin (10% pyrenyl-actin) samples, previously exposed to 15d-PGJ_2. Key: native actin (●); 1:5 actin:15d-PGJ_2 molar ratio (◇); 1:10 actin:15d-PGJ_2 molar ratio (□), and 1:20 actin:15d-PGJ_2 molar ratio (○). All data points represent the mean of two independent determinations.

showed about 28%, 32%, and 45% inhibition in the G-actin samples exposed to 1:5, 1:10, or 1:20 actin:15d-PGJ_2 molar ratio, respectively.

Covalent Binding of 15d-PGJ_2 to Actin: Direct Infusion ESI-MS Analysis. Figure 5A reports the positive ion ESI mass spectrum of native actin showing multiple charged peaks ranging from *m*/*z* 723.1 to *m*/*z* 1497.0 (addition of 58 to 28 protons). To further enhance the MS resolution, a narrow scan range *m*/*z* 1300−1420 was used in order to acquire the MS spectrum for 10 min at a resolution of *m*/*z* 0.5. Figure 5B shows the ESI mass spectrum in the scan range *m*/*z* 1300−1420 relative to native actin, which is characterized by two series of ions attributed to +32, +31, and +30 multicharge ions. The deconvoluted spectrum (right box) shows a main peak (A) at 41872 Da, in good agreement with the theoretical value relative to the N-terminal acetylated α-actin with one methylated His residue of 41873 (SwissProt entry number P68136), thus exhibiting a good accuracy. The second peak at 41958 Da (B, 25% of peak A) is attributed to an actin endogenous complex, very likely the +2 (Ca^{2+}) ion complex.

When actin was incubated in the presence of 15d-PGJ_2 at a molar ratio 1:5 for 1 h at 37 °C, an additional ion series (C) is detectable whose relative abundance (≈8% with respect to native actin) significantly increases with the increase of the actin:15d-PGJ_2 molar ratio, ≈15% at the molar ratio 1:10 (Figure 5C). Deconvolution analysis indicates a MW of 42190 (+318 Da with respect to native actin; theoretical mass increment +318.44 Da), attributed to the reduced 15d-PGJ_2−Michael adduct. At the highest molar ratio (1:20), the deconvoluted peak C shows a relative abundance of 33% with respect to the unmodified actin (data not shown).

Identification of the 15d-PGJ_2 Modification Site by LC-ESI-MS/MS: Peptide Mass Mapping. To characterize the structural modification of actin by 15d-PGJ_2, the native and the 15d-PGJ_2-treated protein were reduced by $NaBH_4$, an established procedure for adduct stabilization (*20*, *21*), digested with trypsin, and then analyzed by LC-ESI-MS/

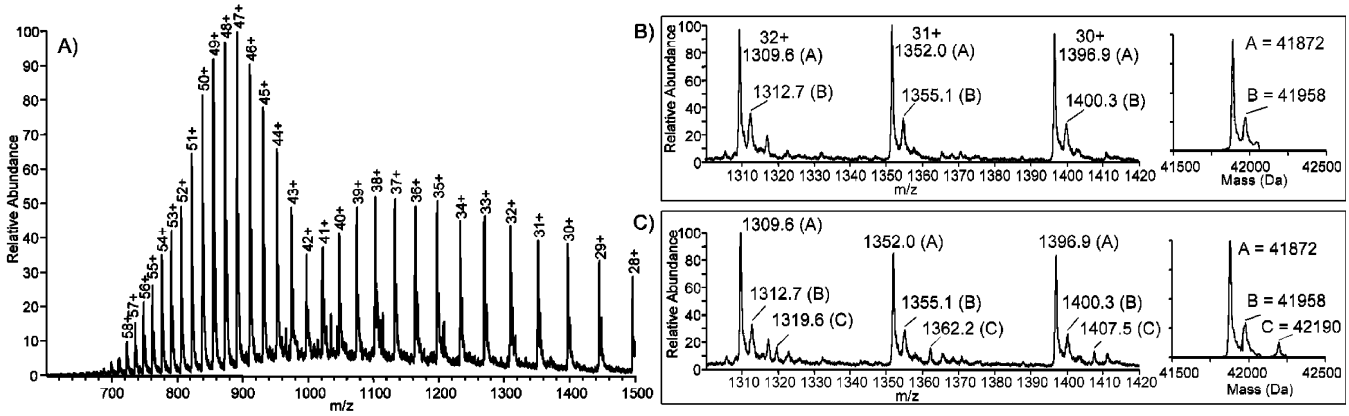

FIGURE 5: Positive ion ESI mass spectra of native and 15d-PGJ$_2$-treated actin (infusion experiments). (A) Native actin (mass range *m*/*z* 600−1500; $Q = m/z$ 1). (B) Native actin (mass range *m*/*z* 1310−1420; $Q = m/z$ 0.5). The right box shows the deconvoluted spectrum. (C) 15d-PGJ$_2$-treated actin (1:10 molar ratio; mass range *m*/*z* 1310−1420; $Q = m/z$ 0.5). The right box shows the deconvoluted spectrum.

MS. Peptide mass mapping of native actin provided identification of the peptides accounting for approximately 83% of the protein sequence. Ion mapping is an useful mass spectrometric tool which can be applied for the rapid identification of covalently adducted peptides, when a diagnostic fragment (neutral or charged) is known: for example, the neutral loss of 158 Da (due to a retro-Michael fragmentation reaction) is used to identify Cys-containing peptides adducted by HNE through a Michael addition. This approach has been successfully applied to unequivocally identify Cys374-Phe375 as the target peptide of HNE-adducted actin (*18*). Since 15d-PGJ$_2$ has been recently found to preferentially react with Cys protein residues (*22*, *23*), and by considering that actin contains five Cys residues in the reduced form (the most accessible and reactive being Cys374) (*18*), as a first step we searched for 15d-PGJ$_2$-modified Cys-containing peptides by using the ion mapping approach. However, since no data are available on the fragmentation pattern of 15d-PGJ$_2$ adducted to Cys-containing peptides in both native and $NaBH_4$-reduced form, the GSH−15d-PGJ$_2$ Michael adduct was prepared and used as a model to identify the diagnostic fragment for the ion mapping search (LC-MS/MS, in both negative and positive ion modes).

The GSH−15d-PGJ$_2$ adduct (1 nmol on the column) elutes at 82.2 min, giving abundant $[M + H]^+$ and $[M - H]^-$ ions at *m*/*z* 624.4 and *m*/*z* 622.7, respectively. The MS2 spectra (data-dependent scan mode) are dominated by the retro-Michael reaction products: the ions at *m*/*z* 307.9 $[M + H -$ 15d-PGJ$_2]^+$ and *m*/*z* 317 $[M + H - GSH]^+$ in the positive ion mode and at *m*/*z* 306 $[M - H -$ 15d-PGJ$_2]^-$ in the negative ion mode (data not shown). As reasonably expected (*24*), the MS and MS2 fragmentation patterns of the $NaBH_4$-reduced adducted peptide (retention time 79.8 min) are significantly different: in the positive ion mode the $[M + H]^+$ ion at *m*/*z* 626.2 is accompanied by the $[M + H - H_2O]^+$ ion (30% relative abundance) at *m*/*z* 608.6. No fragments are obtained from the ion at *m*/*z* 626.2, indicating high instability of the molecular ion in the gas phase. By contrast, the ion at *m*/*z* 608.6 gives as main products the ions at *m*/*z* 301.0 $[15d\text{-}PGJ_2 + H - H_2O]^+$ due to the loss of GSH and at *m*/*z* 283.1, arising by a further loss of water (data not shown). In the negative ion mode the $[M - H]^-$ at *m*/*z* 624.7 gives the product ions at *m*/*z* 607.2 $[M - H - NH_3]^-$ and at

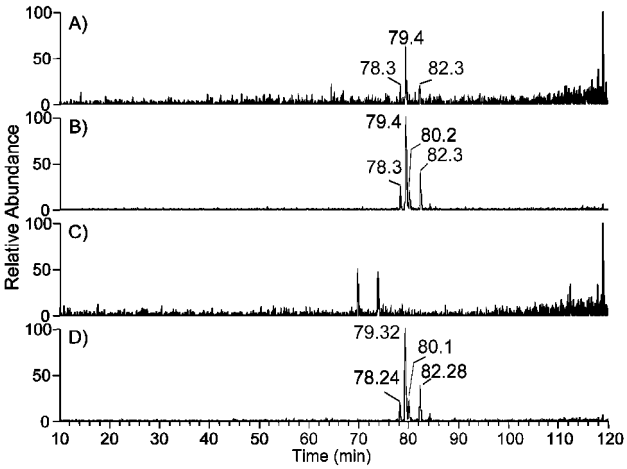

FIGURE 6: LC-ESI-MS/MS analysis of the reduced GSH-15d-PGJ$_2$ adduct (SICs relative to the ion at *m*/*z* 626.2). (A) SIC trace obtained by injection of 20 pmol of adduct. (B) SIC trace obtained by injection of 100 pmol of adduct. (C) SIC trace obtained by injection of 100 pmol of adduct following TCA spiking. (D) SIC trace obtained by injection of 100 pmol of adduct following ultrafiltration.

m/*z* 606.2 $[M - H - H_2O]^-$ and other fragments typical of GSH Michael adducts at *m*/*z* 495.4 $[M - Glu]^-$, *m*/*z* 272 $[GSH - H - H_2S]^-$, and *m*/*z* 254 $[GSH - H - H_2S - H_2O]^-$ (*25*). From these spectrometric analyses it can be concluded that the fragment ion at *m*/*z* 301, arising from the dehydrated ion at *m*/*z* 608.6 (positive ion mode), is a typical product ion of 15d-PGJ$_2$ adducted to Cys-containing peptides and, hence, can be used as the diagnostic ion in the ion mapping analysis.

The reduced GSH−15d-PGJ$_2$ adducted peptide was also used to optimize other critical parameters before analyzing the digested adducted protein and, in particular, the minimal amount of adducted peptide required to obtain a satisfactory ion current and sample preparation. Figure 6 shows the SICs relative to the ion at *m*/*z* 626.2 obtained by injecting 20 pmol (panel A) and 100 pmol (panel B). It is well evident that a satisfactory ion trace is obtained only by injecting 100 pmol: the ion trace shows four distinct peaks attributed to the four diastereoisomers, in accord with the insertion of two new chiral centers. By considering (a) the amount of incubated actin (20 μM), (b) the relative amount of 15d-PGJ$_2$-adducted protein (no more than 35%), and (c) the dilution factor after tryptic digestion (1:2), we can assume

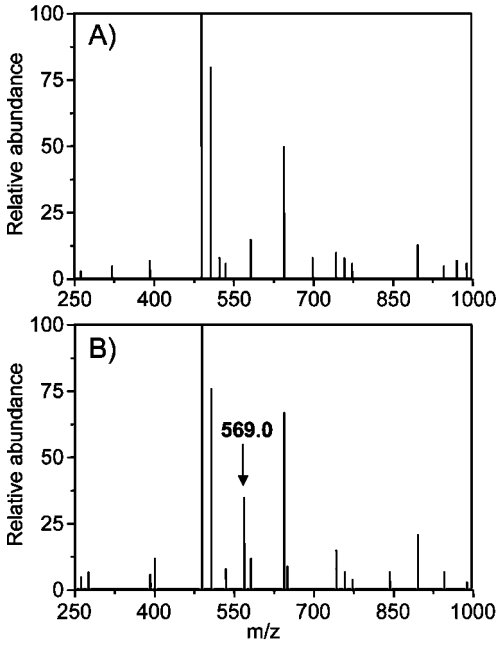

FIGURE 7: Identification of 15d-PGJ_2 adducted peptide by ion mapping. Reconstructed ion maps (product ion *m*/*z* 301) obtained by LC-ESI-MS/MS analysis of native (A) and 15d-PGJ_2-treated actin (B) after trypsin digestion. The ion maps consist of all the parent ions that give products within the selected product ion. The results are relative to the 1:20 actin:15d-PGJ_2 sample.

that by injecting 10 μL of sample the final amount of the adducted peptide on the column would be $\approx$ 30 pmol, an amount barely detectable. To overcome this problem, a 10-fold sample concentration was carried out on-line using a C18 trap cartridge installed in the rheodyne injection valve loop.

Regarding sample preparation, a typical procedure to terminate trypsin digestion involves TCA (10% solution) spiking. However, the addition of TCA to the GSH−15d-PGJ_2 adduct (100 pmol injected) results in a total disappearance of the four peaks (Figure 6C), probably due to the reduced solubility in acidic conditions. Because ultrafiltration does not induce the peptide loss (Figure 6D), this sample preparation was adopted for digested-actin sample preparation. Figure 7 shows the ion map for the selected ion fragment mass *m*/*z* 301.0, relative to the tryptic peptides of native (panel A) and 15d-PGJ_2-treated actin (panel B). These reconstructed spectra consist of all the parent ions (isolated in the data-dependent scan mode) that give products within the product ion of *m*/*z* 301 ($\pm$1 tolerance). Both spectra are characterized by several parent ions and differ only for the presence of the precursor ion at *m*/*z* 569.0 in digested modified actin, tentatively attributed to the $[M + H - H_2O]^+$ ion of the 15d-PGJ_2 adducted to the Cys374-Phe375 dipeptide. Confirmation was achieved by reconstituting the SIC traces of the precursor ion at *m*/*z* 569.0 in both native (Figure 8A) and 15d-PGJ_2-treated actin (Figure 8B). A main peak at retention time 99.6 min is detectable only in the 15d-PGJ_2-treated protein, whose full mass spectrum (Figure 8C) shows, besides the ion at *m*/*z* 569, the $[M + H]^+$ ion at *m*/*z* 587.0, in good agreement with the theoretical mass of the reduced 15d-PGJ_2 adducted to the Cys374-Phe375 dipeptide (586.783 Da). The fragmentation behavior of the $[M + H]^+$ ion at *m*/*z* 587.0 (no product ions; Figure 8D) and of the corresponding dehydrated ion at *m*/*z* 569.0 (Figure 8E), with the

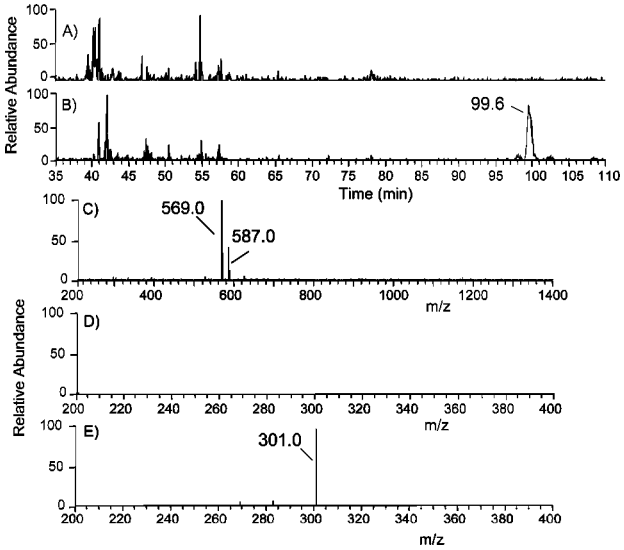

FIGURE 8: LC-ESI-MS/MS analysis of native and 15d-PGJ_2-treated actin after trypsin digestion. (A, B) SICs relative to the ion at *m*/*z* 569.0 in native and 15d-PGJ_2 -treated actin, respectively. (C) MS spectrum of the peak with retention time 99.6. (D) MS/MS spectrum of the parent ion at *m*/*z* 587.0. (E) MS/MS spectrum of the *m*/*z* 587.0 dehydrated ion at *m*/*z* 569.0. The results in panels B−E are relative to the 1:20 actin:15d-PGJ_2 sample.

Table 2: Secondary Structure Motif Abundances (in %) As Monitored during Dynamic Simulations of Native and Both Isomers of 15d-PGJ_2 Actin Adducted on Cys374

secondary motif	0 ns	5 ns		
		native	+(*R*)-15d-PGJ_2	+(*S*)-15d-PGJ_2
α helix	29.3	26.4	19.7	18.8
3_{10} helix	4.8	4.8	1.6	1.5
strand	15.4	17.6	10.4	9.9
turn	34.7	35.6	46.1	47.7
coil	14.4	14.8	20.0	21
bridge	1.3	0.8	1.9	1.1

diagnostic product ion at *m*/*z* 301 $[15d\text{-}PGJ_2 + H - H_2O]^+$, is similar to that found for the Cys model adducted peptide. All of these results confirm that Cys374 is the adduction site on actin for 15d-PGJ_2.

Computational Studies. We considered C-9 as the only adduction site since the 9,10-dihydro-15d-PGJ_2 was found not able to interact with actin (see above). This finding is in line with the work of Suzuki et al. (*26*), who found that the Michael adduction of thiols occurs selectively at the C11 position of Δ^7-PGA_1 methyl ester. A first analysis on MD simulation of the 15d-PGJ_2−actin adduct concerns the RMSD profile as computed considering the backbone atoms only. The obtained results clearly show that both isomers of the 15d-PGJ_2 adduct induce a vast unfolding of actin structure as the RMSD values markedly rise during the entire simulation time and only in the last nanosecond do they seem to reach an equilibrium state (data not shown).

The unfolding process finds a remarkable confirmation when comparing the first and the last frames, as obtained by MD simulation. Thus, the analysis of their secondary structure abundances (computed by STRIDE program, as seen in Table 2) suggests that, while native actin conserves its secondary structure during the entire simulation, the (*R*)-15d-PGJ_2 adduction induces a significant decrease of ordered motifs (namely, helices and strands) counteracted by an

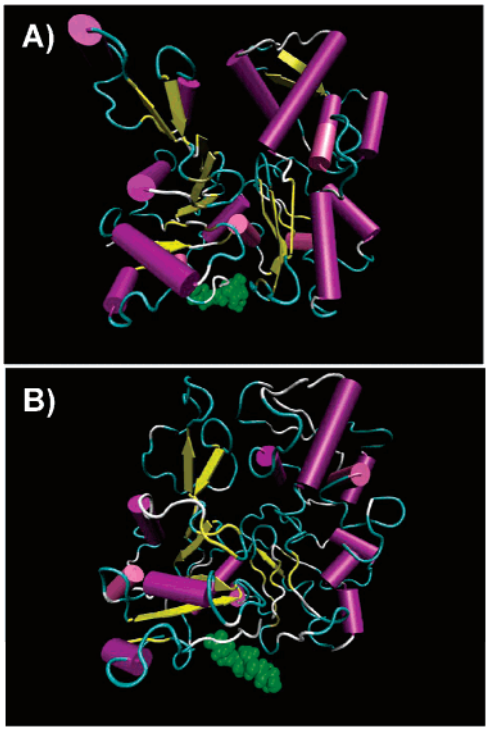

FIGURE 9: 3D representation of actin folding as obtained by MD simulation of the *R* isomer. The structures are depicted as cartons colored by secondary structure (namely, purple = helices, yellow = β-sheets, and azure = coils). In green the (*R*)-15d-PGJ$_2$ is also represented as the CPK model. (A) Actin folding at the beginning of simulation (0 ns). (B) Actin folding at the end of simulation (5 ns).

increase of unfolded structures (namely, turns and coils). An impressive index of actin unfolding can be found considering that more than half (i.e., 53.5%) of the residues change their secondary structure during the simulation.

A visual scrutiny of two structures (namely, the first and the last frame, as seen in Figure 9) shows that the (*R*)-15d-PGJ$_2$ adduct induces a collapse that mainly involves the DNase I binding loop (subdomain 2), which approaches subdomain 4 losing its flexible folding and closing the ATP binding site. In particular, panels A and B of Figure 9 indicate that the unfolding process involves all subdomains, being more evident in subdomains 2 and 3 than in subdomains 1 and 4. A quantitative analysis of the collapse process can be obtained by monitoring the distance values between two residues on the top of subdomains 2 and 4 (for example, Val45 and Asp254) as computed during the MD simulation. Figure 10 shows that the above-mentioned distance markedly decreases during the entire simulation time, ranging from 32 to 11 Å at the end of the simulation. Interestingly, the simulations on the (*S*)-15d-PGJ$_2$ adduct afforded quite identical results (as compiled in Table 2), suggesting that the unfolding effect of 15d-PGJ$_2$ adduction is due to the lipophilic hindrance rather than to specific interactions between 15d-PGJ$_2$ and actin residues.

DISCUSSION

Although there are several reports regarding the effects of 15d-PGJ$_2$ on neuronal cells, the precise mechanisms have not been completely elucidated. In some reports 15d-PGJ$_2$ was found to be neurotoxic and in some others neuroprotective, and it seems that these opposing effects are dependent

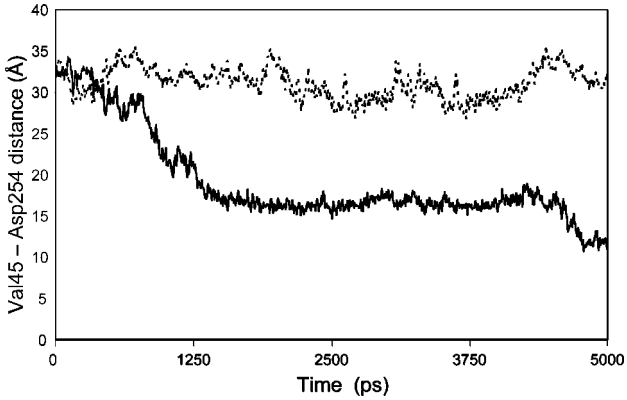

FIGURE 10: Distance profile between Val45 and Asp254 as computed during the MD simulation of the *R* isomer. The residues were selected to quantitate the collapse between subdomains 2 and 3 in the (*R*)-15d-PGJ$_2$ adducted actin. Values were calculated considering the Cα atoms. Key: dashed line, native actin; continuous line, (*R*)-15d-PGJ$_2$ adducted actin.

on the concentration. The neuroprotective effect was observed in a 1−5 μM concentration range (*27*), while the neurotoxicant was at concentrations higher than 10 μM (*28*). More recently, Koh et al. (*29*) confirmed these results since they found that when neuronal cells (N18D3 cells) where treated with 15d-PGJ$_2$, the viability was unaffected up to 8 μM, but decreased at higher concentrations.

The neurotoxic effects of 15d-PGJ$_2$ can be explained by considering several mechanisms. 15d-PGJ$_2$ enhances COX-2 expression by an oxidative shift in the intracellular thiol/disulfide redox state and increases interleukin-1α mRNA levels in the neuronal cells (*28*), impairs the ubiquitin−proteasome pathway by inhibiting ubiquitin C-terminal hydrolase (*30*), and induces apoptosis (*31*). Furthermore, in vitro studies using neuroblastoma cells showed that p53 is a key molecule in the 15d-PGJ$_2$-induced cell apoptosis (*11*).

Regarding the molecular mechanisms, the enzyme inhibition/activation and in general the cellular response induced by 15d-PGJ$_2$ in neuronal cells may be a consequence of covalent binding with cellular proteins, due to the presence of an unsaturated carbonyl group in the cyclopentenone moiety of the molecule, which confers a strong electrophilic nature. Accordingly, Shibata et al. identified thioredoxin 1 as a molecular target for the covalent modification by 15d-PGJ$_2$, providing a biochemical basis for the redox alteration induced by 15d-PGJ$_2$ and hence COX-2 activation (*23*).

To further gain an insight into the role of 15d-PGJ$_2$ covalent modification of protein in neuronal cell dysfunction, the aim of the present study was to use a proteomic approach to identify the main protein target in neuroblastoma cells exposed to cytotoxic concentrations of 15d-PGJ$_2$ (>10 μM).

By using biotinylated 15d-PGJ$_2$, at least 12 proteins were identified as biotin-positive spots, falling in different functional classes, including glycolytic enzymes (enolase and lactate dehydrogenase), redox enzymes (biliverdin reductase), and a eukaryotic regulatory protein (14-3-3γ).

Actin was found as the major target of 15d-PGJ$_2$, thus confirming the high susceptibility of actin among cellular proteins to be modified by reactive electrophilic carbonyls. By using mesangial cells and a proteomic approach, Stamatakis and colleagues recently found that the cellular fate of 15d-PGJ$_2$ is constituted by cytoskeletal proteins, among them actin (*32*). Ozeki and colleagues reported that actin is a major

target of carbonylation by HNE addition in an oxidative stress-induced carcinogenesis model of rats (*33*). Furthermore, many proteomic studies evidenced that actin is one of the main carbonylated proteins in cells and tissues although, in most of these studies, the site of actin adduction as well as the carbonylating agent was not identified (*33*−*39*).

15d-PGJ_2 covalent modification of actin induces marked morphological changes in the actin filament network and, in particular, promotes F-actin depolymerization as confirmed by Western blot analysis. The effect of 15d-PGJ_2 on actin cytoskeleton organization could be mediated by a direct covalent modification of the protein through the electrophilic cyclopentenone binding, as suggested by the nil effect on actin redistribution of 9,10-dihydro-15d-PGJ_2, an analogue of 15d-PGJ_2 that lacks the cyclopentenone moiety.

In order to confirm this hypothesis and to gain a deeper insight into the effects of 15d-PGJ_2 adduction on actin, in the second part of the present work the reaction mechanism as well as the functional effect of the covalent binding of 15d-PGJ_2 on isolated G-actin was studied in an in vitro system. By using a mass spectrometric approach, we found that 15d-PGJ_2 reacts within 60 min with actin in a 1:1 stoichiometric ratio and selectively binds the Cys374 site through a Michael adduction mechanism. The reactivity of Cys374 to unsaturated aldehydes has been previously reported by using HNE (*18*) as well as acrolein (*40*) as models of α,β-unsaturated aldehydes and is due to the significant accessible surface and substantial thiol acidity, due to the particular microenvironment surrounding the amino acid.

Computational studies showed that the covalent binding of 15d-PGJ_2 induces a significant unfolding of actin structure. In particular, MD simulations indicated that 15d-PGJ_2 distorts the actin subdomains 2 and 4, which define the nucleotide binding sites impeding the nucleotide exchange. Moreover, 15d-PGJ_2 occupies a deep cleft between subdomains 1 and 3, which is implicated in contacts with the complementary residues of the neighboring actin monomer in F-actin.

Actin Cys374 has previously been reported to play an important antioxidant role by scavenging damaging reactive molecules/oxidizing agents (*13*, *41*−*43*). Furthermore, considering (i) the relative actin abundance in most mammalian cells, (ii) the high reactivity of the exposed Cys374 sulfhydryl group, which binds electrophilic α,β-unsaturated aldehydes, up to C9, such as acrolein and HNE (*18*, *33*, *44*), without the polymerization process resulting impaired (*40*), and (iii) that actin has been identified as a major cellular target of HNE (*33*) as well as of biotinylated 15d-PGJ_2, in mesangial cells (*32*), it has been proposed that actin Cys374 could potentially compete or cooperate with GSH and histidine-containing dipeptides in the intracellular scavenging of reactive carbonyl species (*40*).

The nil effect of Cys374 actin carbonylation by acrolein and HNE is related to the plasticity of the protein whose covalent modifications induce insignificant conformational shifts that do not change the global actin folding. However, we found that 15d-PGJ_2, which is scavenged by actin, induces a significant conformational distortion and impairs the ability of actin to polymerize. Hence, in the case of 15d-PGJ_2, the plasticity of the segment bearing the Cys374 residue is not sufficient to counteract the steric hindrance of the aldehyde, and this induces molecular distortion and impairment of actin function. Moreover, a second factor that influences the polymerization process is the capacity of adducts to shield the residues involved in interactions with neighboring actin monomers. HNE is a linear molecule that inserts in the actin nucleotide cleft without covering these key residues, while 15d-PGJ_2 is a bulkier adduct that spans a large part of actin surface shielding the residues involved in polymer stabilization. This hypothesis is supported by our preliminary observation that 2-cyclopenten-1-one, possessing the similar reactive moiety as 15d-PGJ_2, did not induce actin redistribution (Supporting Information, Figure S1) as well as any significant unfolding of the protein (data not shown).

Hence, actin Cys374 could be regarded as a molecular buffer of reactive carbonyls from lipid peroxidation, and actin is one of the main cellular targets of 15d-PGJ_2 in human neuroblastoma SH-SY5Y cells. However, contrary to lipid peroxidation-derived reactive carbonyl species, the electrophilic prostaglandin induces conformational distortions, and this can in part explain the effect of 15d-PGJ_2 on actin polymerization, as it is conceivable that 15d-PGJ_2−actin adducts cannot participate to the polymerization process because of structural constraints.

On the other hand, rearrangement of the actin cytoskeleton is controlled by dynamic assembly and disassembly of actin filaments. Regulated disassembly as well as assembly is important for maintaining constant turnover of actin filaments. Tropomyosin, an actin-interacting protein which cooperatively regulates the interaction of actin with myosin heads, has been identified as one of the target proteins of 15d-PGJ_2 (*32*). Since a vast number of actin-interacting proteins direct the location, rate, and timing for actin assembly into different structures, binding of 15d-PGJ_2 to actin-interacting proteins may also result in the impairment of regulated assembly and disassembly of actin filaments.

Several studies found that PGs are produced in the brain and spinal cord in response to different types of challenges (for review see ref *45*). PGD_2 is the major prostanoid made in the CNS (*46*) and readily undergoes dehydration in vivo and in vitro to yield PGJ_2 and its metabolites, Δ^{12}-PGJ_2 and 15d-PGJ_2, without requiring additional enzymatic steps (*4*). Thus, it is likely that 15d-PGJ_2 is produced in the CNS in response to proinflammatory events. Interestingly, the levels of 15d-PGJ_2 are elevated in spinal cord motor neurons of ALS patients (*11*). In the present work we found that actin is the main protein cellular target of 15d-PGJ_2, which specifically binds through a Michael adduction to Cys374, leading to protein conformational changes, which can explain the disruption of the actin cytoskeleton and F-actin depolymerization. These cellular effects have been observed by using concentrations of 15d-PGJ_2 in the micromolar range (10 μM). Although physiological concentrations of PGs are present in body fluids in pico- and nanomolar concentrations (*47*), their levels rise considerably under pathological conditions, such as hyperthermia, infection, and inflammation, and local PG concentration reaching the micromolar range has been detected at the site of damage (*48*). Indeed, several

[2] While this paper was under review, Gayarre et al. (*51*) reported that actin is a target for modification of biotinylated 15d-PGJ_2, Cys374 is the site for interaction, and actin modified by addition of 15d-PGJ_2 forms filaments of altered morphology. Our data are in good agreement with those findings.

previous studies have successfully determined the in vivo levels of the J_2 series of PGs. (i) Hirata et al. (*49*) have detected significant quantities (~150 ng/24 h in human males) of Δ^{12}-PGJ$_2$ in human and monkey urine and larger amounts of other, uncharacterized Δ^{12}-PGJ$_2$ immunoreactive compounds in human urine. (ii) Gilroy et al. (*50*) have observed an elevated level (1000 pg/mL exudate) of 15d-PGJ$_2$ in the late phases of inflammation. (iii) Shibata et al. (*4*) have reported detecting relatively high levels (80 nM) of 15d-PGJ$_2$ in medium from RAW264.7 macrophage-like cells stimulated with lipopolysaccharides.[2]

In summary, the results here reported give an insight into the role of 15d-PGJ$_2$ as a cytotoxic compound in the neuronal cell dysfunction. Actin is the main protein cellular target of 15d-PGJ$_2$ which specifically binds through a Michael adduction to Cys374 leading to a protein conformational change which can explain the disruption of the actin cytoskeleton, F-actin depolymerization, and impairment of G-actin polymerization. Moreover, given the participation of the actin cytoskeleton in cellular motility and division, it would be worthwhile to perform further studies to evaluate 15d-PGJ$_2$ antiproliferative activity/effects against different tumor cell lines and, possibly/in case, using it as a model for the development of a new class of antiproliferative agents.

SUPPORTING INFORMATION AVAILABLE

Effect of 2-cyclopenten-1-one on actin cytoskeleton. SH-SY5Y cells were treated with DMSO (upper), 20 μM 2-cyclopenten-1-one (middle), and 50 μM 2-cyclopentene-1-one (bottom) for 2 h and then stained with phalloidin to visualize filamentous actin. This material is available free of charge via the Internet at http://pubs.acs.org.

REFERENCES

1. Smith, W. L. (1989) The eicosanoids and their biochemical mechanisms of action, *Biochem. J. 259*, 315−324.
2. Smith, W. L. (1992) Prostanoid biosynthesis and mechanisms of action, *Am. J. Physiol. 263*, F181−F191.
3. Giles, H., and Leff, P. (1988) The biology and pharmacology of PGD2, *Prostaglandins 35*, 277−300.
4. Shibata, T., Kondo, M., Osawa, T., Shibata, N., Kobayashi, M., and Uchida, K. (2002) 15-deoxy-delta 12,14-prostaglandin J2. A prostaglandin D2 metabolite generated during inflammatory processes, *J. Biol. Chem. 277*, 10459−10466.
5. Ricote, M., Li, A. C., Willson, T. M., Kelly, C. J., and Glass, C. K. (1998) The peroxisome proliferator-activated receptor-gamma is a negative regulator of macrophage activation, *Nature 391*, 79−82.
6. Jiang, C., Ting, A. T., and Seed, B. (1998) PPAR-gamma agonists inhibit production of monocyte inflammatory cytokines, *Nature 391*, 82−86.
7. Rossi, A., Kapahi, P., Natoli, G., Takahashi, T., Chen, Y., Karin, M., and Santoro, M. G. (2000) Anti-inflammatory cyclopentenone prostaglandins are direct inhibitors of IkappaB kinase, *Nature 403*, 103−108.
8. Straus, D., Pascual, G., Li, M., Welch, J. S., Ricote, M., Hsiang, C. H., Sengchanthalangsy, L. L., Ghosh, G., and Glass, C. K. (2000) 15-deoxy-delta 12,14-prostaglandin J2 inhibits multiple steps in the NF-kappa B signaling pathway, *Proc. Natl. Acad. Sci. U.S.A. 97*, 4844−4849.
9. Bishop-Bailey, D., and Hla, T. (1999) Endothelial cell apoptosis induced by the peroxisome proliferator-activated receptor (PPAR) ligand 15-deoxy-delta12,14-prostaglandin J2, *J. Biol. Chem. 274*, 17042−17048.
10. Kawamoto, Y., Nakamura, Y., Naito, Y., Torii, Y., Kumagai, T., Osawa, T., Ohigashi, H., Satoh, K., Imagawa, M., and Uchida, K. (2000) Cyclopentenone prostaglandins as potential inducers of phase II detoxification enzymes. 15-deoxy-delta(12,14)-prostaglandin J2-induced expression of glutathione S-transferases, *J. Biol. Chem. 275*, 11291−11299.
11. Kondo, M., Shibata, T., Kumagai, T., Osawa, T., Shibata, N., Kobayashi, M., Sasaki, S., Iwata, M., Noguchi, N., and Uchida, K. (2002) 15-Deoxy-delta(12,14)-prostaglandin J(2): the endogenous electrophile that induces neuronal apoptosis, *Proc. Natl. Acad. Sci. U.S.A. 99*, 7367−7372.
12. Cernuda-Morollon, E., Pineda-Molina, E., Canada, F. J., and Perez-Sala, D. (2001) 15-Deoxy-delta 12,14-prostaglandin J2 inhibition of NF-kappaB-DNA binding through covalent modification of the p50 subunit, *J. Biol. Chem. 276*, 35530−35536.
13. Dalle-Donne, I., Milzani, A., and Colombo, R. (1999) The tert-butyl hydroperoxide-induced oxidation of actin Cys-374 is coupled with structural changes in distant regions of the protein, *Biochemistry 38*, 12471−12480.
14. Kouyama, T., and Mihashi, K. (1981) Fluorimetry study of N-(1-pyrenyl)iodoacetamide-labelled F-actin. Local structural change of actin protomer both on polymerization and on binding of heavy meromyosin, *Eur. J. Biochem. 114*, 33−38.
15. Cooper, J. A., Walker, S. B., and Pollard, T. D. (1983) Pyrene actin: documentation of the validity of a sensitive assay for actin polymerization, *J. Muscle Res. Cell Motil. 4*, 253−262.
16. Zhang, Z., and Marshall, A. G. (1998) A universal algorithm for fast and automated charge state deconvolution of electrospray mass-to-charge ratio spectra, *J. Am. Soc. Mass Spectrom. 9*, 225−233.
17. Wilkins, M. R., Lindskog, I., Gasteiger, E., Bairoch, A., Sanchez, J. C., Hochstrasser, D. F., and Appel, R. D. (1997) Detailed peptide characterization using PEPTIDEMASS−a World-Wide-Web-accessible tool, *Electrophoresis 18*, 403−408.
18. Aldini, G., Dalle-Donne, I., Vistoli, G., Maffei Facino, R., and Carini, M. (2005) Covalent modification of actin by 4-hydroxy-trans-2-nonenal (HNE): LC-ESI-MS/MS evidence for Cys374 Michael adduction, *J. Mass Spectrom. 40*, 946−954.
19. Pedretti, A., Villa, L., and Vistoli, G. (2002) VEGA: a versatile program to convert, handle and visualize molecular structure on Windows-based PCs, *J. Mol. Graphics Modell. 21*, 47−49.
20. Crabb, J. W., O'Neil, J., Miyagi, M., West, K., and Hoff, HF. (2002) Hydroxynonenal inactivates cathepsin B by forming Michael adducts with active site residues, *Protein Sci. 11*, 831−840.
21. Fenaille, F., Guy, P. A., and Tabet, J. C. (2003) Study of protein modification by 4-hydroxy-2-nonenal and other short chain aldehydes analyzed by electrospray ionization tandem mass spectrometry, *J. Am. Soc. Mass Spectrom. 14*, 215−226.
22. Ishii, T, and Uchida, K. (2004) Induction of reversible cysteine-targeted protein oxidation by an endogenous electrophile 15-deoxy-delta12,14-prostaglandin J2, *Chem. Res. Toxicol. 17*, 1313−1322.
23. Shibata, T., Yamada, T., Ishii, T., Kumazawa, S., Nakamura, H., Masutani, H., Yodoi, J., and Uchida, K. (2003) Thioredoxin as a molecular target of cyclopentenone prostaglandins, *J. Biol. Chem. 278*, 26046−26054.
24. Oberth, C. H., and Jones, A. D. (1997) Fragmentation of protonated thioether conjugates of acrolein using low collision energies, *J. Am. Soc. Mass Spectrom. 8*, 727−736.
25. Aldini, G., Granata, P., Orioli, M., Santaniello, E., and Carini, M. (2003) Detoxification of 4-hydroxynonenal (HNE) in keratinocytes: characterization of conjugated metabolites by liquid chromatography/electrospray ionization tandem mass spectrometry, *J. Mass Spectrom. 38*, 1160−1168.
26. Suzuki, M., Mori, M., Niwa, T., Hirata, R., Furuta, K., Toshihisa, I., and Noyori, R. (1997) Chemical implications for antitumor and antiviral prostaglandins: reaction of 7-prostaglandin A1 and prostaglandin A1 methyl esters with thiols, *J. Am. Chem. Soc. 119*, 2376−2385.
27. Aoun, P., Simpkins, J. W., Agarwal, N. (2003) Role of PPAR-gamma ligands in neuroprotection against glutamate-induced cytotoxicity in retinal ganglion cells, *Invest. Ophthalmol. Visual Sci. 44*, 2999−3004.
28. Li, Z., Jansen, M., Ogburn, K., Salvatierra, L., Hunter, L., Mathew, S., and Figueiredo-Pereira, M. E. (2004) Neurotoxic prostaglandin J2 enhances cyclooxygenase-2 expression in neuronal cells through the p38MAPK pathway: a death wish?, *J. Neurosci. Res. 78*, 824−836.
29. Koh, S. H., Jung, B., Song, C. W., Kim, Y., Kim, Y. S., and Kim, S. H. (2005) 15-Deoxy-delta12,14-prostaglandin J2, a neuroprotectant or a neurotoxicant?, *Toxicology 216*, 232−243.

30. Li, Z., Melandri, F., Berdo, I., Jansen, M., Hunter, L., Wright, S., Valbrun, D., and Figueiredo Pereira, M. E. (2004) Delta12-prostaglandin J2 inhibits the ubiquitin hydrolase UCH-L1 and elicits ubiquitin-protein aggregation without proteasome inhibition, *Biochem. Biophys. Res. Commun. 319*, 1171−1180.
31. Rohn, T. T., Wong, S. M., Cotman, C. W., and Cribbs, D. H. (2001) 15-deoxy-delta12,14-prostaglandin J2, a specific ligand for peroxisome proliferator-activated receptor-gamma, induces neuronal apoptosis, *Neuroreport 12*, 839−843.
32. Stamatakis, K., Sanchez-Gomez, F. J., and Perez-Sala, D. (2006) Identification of novel protein targets for modification by 15-deoxy-delta12,14-prostaglandin J2 in mesangial cells reveals multiple interactions with the cytoskeleton, *J. Am. Soc. Nephrol. 17*, 89−98.
33. Ozeki, M., Miyagawa-Hayashino, A., Akatsuka, S., Shirase, T., Lee, W., Uchida, K., and Toyokuni, S. (2005) Susceptibility of actin to modification by 4-hydroxy-2-nonenal, *J. Chromatogr. B 827*, 119−126.
34. Aksenov, M. Y., Aksenova, M. V., Butterfield, D. A., Geddes, J. W., and Markesbery, W. R. (2001) Protein oxidation in the brain in Alzheimer's disease, *Neuroscience 103*, 373−383.
35. Canton, M., Neverova, I., Menabò, R., Van Eyk, J., and Di Lisa, F. (2004) Evidence of myofibrillar protein oxidation induced by postischemic reperfusion in isolated rat hearts, *Am. J. Physiol. Heart Circ. Physiol. 286*, H870−H877.
36. Oh-Ishi, M., Ueno, T., and Maeda, T. (2003) Proteomic method detects oxidatively induced protein carbonyls in muscles of a diabetes model Otsuka Long-Evans Tokushima Fatty (OLETF) rat, *Free Radical Biol. Med. 34*, 11−22.
37. Keshavarzian, A., Banan, A., Farhadi, A., Komanduri, S., Mutlu, E., Zhang, Y., and Fields, J. Z. (2003) Increases in free radicals and cytoskeletal protein oxidation and nitration in the colon of patients with inflammatory bowel disease, *Gut 52*, 720−728.
38. Barreiro, E., Gea, J., Di Falco, M., Kriazhev, L., James, S., and Hussain, S. N. (2005) Protein carbonyl formation in the diaphragm, *Am. J. Respir. Cell. Mol. Biol. 32*, 9−17.
39. Poon, H. F., Vaishnav, R. A., Getchell, T. V., Getchell, M. L., and Butterfield, D. A. (2006) Quantitative proteomics analysis of differential protein expression and oxidative modification of specific proteins in the brains of old mice, *Neurobiol. Aging 27*, 1010−1019.
40. Dalle-Donne, I., Carini, M., Vistoli, G., Gamberoni, L., Giustarini, D., Colombo, R., Maffei Facino, R., Rossi, R., Milzani, A., and Aldini, G. (2006) Actin Cys374 as a nucleophilic target of α,β-unsaturated aldehydes, *Free Radical Biol. Med.* (doi:10.1016/j.freeradbiomed.2006.11.026).
41. Dalle-Donne, I., Milzani, A., Giustarini, D., Di Simplicio, P., Colombo, R., and Rossi, R. (2000) S-NO-actin: S-nitrosylation kinetics and the effect on isolated vascular smooth muscle, *J. Muscle Res. Cell Motil. 21*, 171−181.
42. Dalle-Donne, I., Giustarini, D., Rossi, R., Colombo, R., and Milzani, A. (2003) Reversible S-glutathionylation of Cys 374 regulates actin filament formation by inducing structural changes in the actin molecule, *Free Radical Biol. Med. 34*, 23−32.
43. Chen, F., and Ogut, O. (2006) Captopril prevents myosin light chain phosphatase isoform switching to preserve normal cGMP-mediated vasodilatation, *Am. J. Physiol. Cell. Physiol. 290*, C719−C727.
44. Usatyuk, P. V., and Natarajan, V. (2004) Role of mitogen-activated protein kinases in 4-hydroxy-2-nonenal-induced actin remodeling and barrier function in endothelial cells, *J. Biol. Chem. 279*, 11789−11797.
45. Kaufmann, W. E., Andreasson, K. I., Isakson, P. C., and Worley, P. F. (1997) Cyclooxygenases and the central nervous system, *Prostaglandins 54*, 601−624.
46. Urade, Y., Hayaishi, O., Matsumura, H., and Watanabe, K. (1996) Molecular mechanism of sleep regulation by prostaglandin D2, *J. Lipid Mediat. Cell Signal. 14*, 71−82.
47. Fukushima, M. (1990) Prostaglandin J2—anti-tumour and anti-viral activities and the mechanisms involved, *Eicosanoids 3*, 189−99.
48. Herschman, H., Gilbert, R., Reddy, S., and Xie, W. L. (1997) Coordinate regulation of the inducible forms of prostaglandin synthase and nitric oxide synthase in fibroblasts and macrophages, *Adv. Exp. Med. Biol. 400A*, 177−182.
49. Hirata, Y., Hayashi, H., Ito, S., Kikawa, Y., Ishibashi, M., Sudo, M., Miyazaki, H., Fukushima, M., Narumiya, S., and Hayashi, O. (1988) Occurrence of 9-deoxy-Δ^9,Δ^{12}−13,14-dihydroprostaglandin D_2 in human urine, *J. Biol. Chem. 263*, 16619−16625.
50. Gilroy, D. W., Colville-Nash, P. R., Willis, D., Chivers, J., Paul-Clark, M. J., and Willoughby, D. A. (1999) Inducible cyclooxygenase may have anti-inflammatory properties, *Nat. Med. 5*, 698−701.
51. Gayarre, J., Sanchez, D., Sanchez-Gomez, F. J., Terron, M. C., Llorca, O., and Perez-Sala, D. (2006) Addition of electrophilic lipids to actin alters filament structure, *Biochem. Biophys. Res. Commun. 349*, 1387−1393.

BI0618565